

Suppressed charge recombination in hematite photoanode *via* protonation and annealing

Wenping Si,^{*,†‡} Fatima Haydous,[†] Ugljesa Babic,[§] Daniele Pergolesi,[†] and Thomas Lippert^{*,†,⊥}

[†] Thin Films and Interfaces, Research with Neutrons and Muons Department, Paul Scherrer Institut, 5232 Villigen PSI, Switzerland

[‡] Key Laboratory of Advanced Ceramics and Machining Technology, Ministry of Education, School of Materials Science and Engineering, Tianjin University, Tianjin 300072, P.R. China

[§] Electrochemistry Laboratory, Paul Scherrer Institut, 5232 Villigen-PSI, Switzerland

[⊥] Laboratory of Inorganic Chemistry, Department of Chemistry and Applied Biosciences, ETH Zurich, 8093 Zurich, Switzerland

●, *Supporting Information*

ABSTRACT

Hematite as promising photoanode for solar water splitting suffers from severe bulk and surface charge recombination. This work describes that a protonation-annealing treatment can effectively

suppress both bulk and surface charge recombination in hematite. Protons/electrons are electrochemically incorporated into hematite under 0.2 V_{RHE} followed by annealing at 120 °C. The photocurrent density increases from ~0.9 mA cm⁻² to 1.8 mA cm⁻² at 1.23 V_{RHE} under 1 sun, and further to 2.7 mA cm⁻² after loading cobalt phosphate, stabilizing at round 2.4 mA cm⁻². A cathodic shift of the onset potential of photocurrent is also observed. H₂O₂ oxidation, impedance spectroscopy and Mott-Schottky measurements show that the protonation suppresses bulk recombination and enhances donor density, but introducing more surface recombination. The annealing reduces surface recombination, while preserving relatively high bulk charge separation efficiency. Different from previous reports on the electrochemically reduced hematite, this work demonstrates that the performance improvement should be ascribed to the proton incorporation instead of the formation of Fe₃O₄ or metal Fe. This facile treatment by protonation and annealing could be applied in other semiconductors to promote the development of high performing photoelectrodes.

KEYWORDS: hematite photoanode, photoelectrochemical water splitting, electrochemical doping, proton incorporation, protonation and annealing, suppressed charge recombination

1. INTRODUCTION

The photoelectrochemical (PEC) splitting of water into hydrogen and oxygen is an attractive approach for converting solar energy into chemical fuels.¹⁻² Photons absorbed by a semiconductor create electron-hole pairs, which can be separated by the space charge layer of the semiconductor to reduce/oxidize water into hydrogen and oxygen at the electrode-electrolyte interface. Hematite (α -Fe₂O₃) has been intensively examined as photoanode for PEC water splitting³⁻¹² due to its

theoretically high solar-to-hydrogen conversion efficiency (14–17%, corresponding to a photocurrent density of 11–14 mA cm⁻² at 1.23 V_{RHE} under 100 mW cm⁻² irradiation).¹³⁻¹⁵ However, the reported photocurrent densities for water splitting using hematite photoanodes are far below the theoretical maximum value.^{4-5, 7, 16-19} Only the electron-hole pairs which are photo-generated within the space charge layer or those can diffuse into this layer will be separated, while the rest of the electron-hole pairs will recombine in the bulk.^{8, 13} Moreover, severe surface recombination has also been reported due to the photo-induced high valent iron species at the surface.²⁰⁻²¹

Various morphologies of hematite photoanodes on fluorine-doped tin oxide (FTO) substrate have been reported including hydrothermally prepared nanorods,^{4-5, 10, 16-18} solution-based colloids,³ chemical vapor deposited nanostructures,^{7, 22-25} spray pyrolyzed platelets²³ and deposition-annealing prepared nanoparticles.¹⁹ According to literature,^{4-5, 16-18} hydrothermally prepared hematite nanorods need to be activated by a short time annealing at about 800 °C to enable tin diffusion into hematite from FTO substrate for higher donor density and better interface between hematite and FTO. Photocurrent densities^{4-5, 17-18} with a large dispersion have been reported in the range of 0.6–1.3 mA cm⁻² for hematite nanorod photoanodes at 1.23 V_{RHE}, while loading cocatalysts NiFeO_x⁴ or FeOOH⁵ improves the photocurrent density to ~1.4 mA cm⁻². Doping with Zr¹⁶, Pt¹⁸ and P²⁶ results in higher photocurrent density of ~1.5 mA cm⁻², ~2.2 mA cm⁻² and ~2.7 mA cm⁻², which can be further increased up to over 3 mA cm⁻² after loading cobalt phosphate (Co-Pi) cocatalyst. An extra passivation layer of SiO_x²⁷, TiO₂²⁸ or Fe₂TiO₅²⁹ deposited by atomic layer deposition also demonstrates significant improvement in the PEC performance of hematite photoanode.

A negative polarization of metal oxide electrodes in aqueous electrolyte can simultaneously introduce electrons and small cations such as H⁺ and Li⁺ in the bulk structure, which is termed

electrochemical doping.³⁰⁻³⁶ The incorporation of proton/e⁻ was found to improve the electrode efficiency for dye-sensitized solar cells³²⁻³³ and water splitting.^{30, 34-35} Proton functions as a shallow donor in semiconductors and increases the donor density, thus improving the majority carrier transport, as demonstrated for semiconductors with low donor densities like WO₃,³⁰ TiO₂,³²⁻³³ ZnO,³⁷ In₂O₃ and SnO₂,³⁸ *etc.* Moreover, another reason for the improved photocurrent has been recently clarified that electrochemically incorporated protons readily segregates to the grain boundary reducing 50% of the overall number of deep electron traps.³¹ The protonation through electrochemical doping is usually long lasting and can only be reversed by extremely long time positive polarization³¹ or heating at high temperature.³⁰ On the other hand, a negative enough polarization can also reduce hematite to more conductive phases such as Fe₃O₄ or even Fe to enhance the performances.^{34, 39-40}

This study aims at understanding the influence of electrochemical doping on the PEC performance of hematite nanorods photoanode prepared by hydrothermal method.^{4-5, 16-18, 41} Protons are electrochemically introduced to hematite, followed by annealing treatments at an optimized temperature of 120 °C. Indeed, the protonation and annealing processed hematite shows a photocurrent density of 1.8 mA cm⁻² at 1.23 V_{RHE}, which is higher than the values reported in literature for hematite nanorods photoanode without cocatalysts.^{4-5, 16-17} After loading Co-Pi cocatalyst, hematite exhibits a photocurrent density of 2.7 mA cm⁻² at 1.23 V_{RHE}, which stabilizes at around 2.4 mA cm⁻² after 5 h test, comparable to the performances previously reported for hematite with different morphologies such as Ti-doped hematite nanoparticles,¹⁹ IrO₂-loaded hematite cauliflowers.⁷ XPS, Raman and Mössbauer spectra excludes the presence of Fe²⁺ or Fe. Thus we ascribe the photocurrent change to the incorporation of proton/e⁻, which is similar to the Volmer reaction for hydrogen evolution reaction. We clarify that the protonation improves the

bulk charge separation efficiency but introduces more surface recombination, while the annealing treatment suppresses the surface recombination, still preserving relatively high bulk charge separation efficiency.

2. EXPERIMENTAL SECTION

2.1. Preparation of hematite photoanode. Fluorine-doped tin oxide (FTO) glass substrates ($6\sim 9 \Omega \text{ sq}^{-1}$, Xop Glass) were cleaned by deionized water, isopropanol and acetone. β -FeOOH nanorods were grown on FTO in a solution containing 0.15 M FeCl_3 (97%, Aldrich) and 1 M NaNO_3 (99.5%, Merck) with a pH 1.5 adjusted by HCl. The reaction was carried out at 100 °C for 6 h. Kapton tape was used to define the area for hematite growth and isolate the back side of the glass from the growing solution. After removing Kapton tapes and cleaning with DI water, FeOOH was annealed in air at 550 °C for 2 h and then activated by annealing at 800 °C for 10 min in a tube furnace to enable the diffusion of Sn from fluorine-doped SnO_2 (FTO) substrate to hematite.^{4-5, 16-}

18

2.2. Co-Pi deposition. The layer of Co-Pi on annealed hematite was loaded by photo-assisted electrodeposition under AM 1.5 G illumination from an electrolyte containing 0.5 mM $\text{Co}(\text{NO}_3)_2 \cdot 6\text{H}_2\text{O}$ (98%, Alfa Aesar) in 0.1 M potassium phosphate buffer at pH 7. A galvanostatic deposition was applied for 100 s with a current density of $6 \mu\text{A cm}^{-2}$.

2.3. Photoelectrochemical characterization. All photoelectrochemical measurements were performed using a potentiostat/galvanostat Solartron 1286 electrochemical interface. The light source was a 150 W Xenon arc lamp equipped with an AM 1.5 G filter (100 mW cm^{-2} , Newport 66477-150XF-R1) calibrated by a photodetector (Gentec-EO). PEC measurements were performed in a three electrode configuration in a quartz cell in Ar-saturated 0.5 M NaOH (pH=13.0)

electrolyte. Hematite/FTO photoelectrode was used as the working electrode, a Pt mesh and Ag/AgCl were used as the counter and the reference electrodes, respectively. Potentiodynamic measurements with a scan rate of 10 mV s^{-1} in the potential window of 0.4–1.6 V_{RHE} were performed to probe the photocurrents.

Open-circuit potentials were measured in O_2 -saturated 0.5 M NaOH electrolyte, and each dark/light potential reading was obtained after stabilization for at least 30 min with oxygen gas bubbling into the electrolyte.

2.4. Impedance spectroscopy and Mott-Schottky plots. Dark and light impedance spectroscopy measurements were carried out in O_2 -saturated 0.5 M NaOH electrolyte on a Solartron 1260 impedance analyzer combined with potentiostat Solartron 1286 in the frequency range between 10 mHz and 10 kHz using 5 mV AC amplitude. Mott-Schottky plots were obtained by fitting the dark impedance spectroscopy data. The sampling was taken every 50 mV in the potential region of 0.78-1.18 V_{RHE} , and prior to impedance measurement, hematite was stabilized at the measuring potential for 30 min. Light impedance spectroscopy was carried out at 1.18 V_{RHE} and 0.98 V_{RHE} under AM 1.5 G illumination. Data analysis was performed with ZView software.

2.5. Materials characterizations. The surface morphology of hematite was examined with a scanning electron microscope (SEM, Ultra 55, Carl Zeiss) operated at an accelerating voltage of 10 kV. X-ray photoelectron spectroscopy (XPS) measurements were done using a VG ESCALAB 220iXL spectrometer (Thermo Fischer Scientific) equipped with an Al $K\alpha$ monochromatic source and a magnetic lens system. Mössbauer spectroscopy was done with conversion electron Mössbauer spectroscopy mode (CEMS) with electrons of about 5-10 keV. Raman spectra were recorded on Labram confocal Raman spectroscopy system, Jobin Yvon. X-ray diffraction (XRD)

measurements were conducted by a Bruker–Siemens D500 X-ray Diffractometer. AFM was conducted on Agilent AFM5500 scanning probe microscope.

3. RESULTS AND DISCUSSION

3.1. PEC performance of hematite. Hematite nanorods on FTO were obtained by annealing the hydrothermally grown β -FeOOH nanorods in air at 550 °C for 2 h and then at 800 °C for 10 min. The as-prepared hematite shows a photocurrent density of $\sim 0.9 \text{ mA cm}^{-2}$ at 1.23 V_{RHE} , and $\sim 1.6 \text{ mA cm}^{-2}$ at 1.6 V_{RHE} , which are similar to previous reports in Ref. 4-5, 16.

The same hematite was then polarized at a slightly negative potential of 0.2 V_{RHE} ($-0.78 \text{ V vs. Ag/AgCl}$) for 200 s to incorporate proton/ e^- couples (protonation). After the 1st protonation, at highly positive potentials the hematite shows higher photocurrent densities than the as-prepared one (Figure 1a), but has lower photocurrent densities than the as-prepared one at moderately positive potentials between $\sim 1.0 V_{\text{RHE}}$ and $\sim 1.35 V_{\text{RHE}}$.

After protonation, hematite was annealed in air under a temperature of 120 °C for 1 h. Temperature and time were optimized by a series of annealing test under various temperature from 80 °C to 250 °C for different time (see Supporting Information Figure S1). This annealing treatment can improve photocurrent densities throughout the whole scanned potential region. It is worth mentioning that no color changes were observed between the as-prepared, protonated and annealed hematite, which has reddish orange color as shown in Figure S2a.

After the 2nd protonation process, the photocurrent density curve of hematite shows similar features as that of the 1st protonated hematite. Only under highly positive potentials, the 2nd protonated hematite has higher photocurrent densities than the 1st annealed hematite. Again, the

2nd annealed hematite shows a further overall improvement throughout the whole scanned potentials compared to the 1st annealed hematite. After these two rounds of protonation/annealing treatment, hematite has a photocurrent density of 1.8 mA cm⁻² at 1.23 V_{RHE}, twice of that for as-prepared hematite. In addition, the photocurrent onset potential is negatively shifted by ~80 mV in comparison to the as-prepared hematite. It is also noteworthy that the 2nd protonated hematite exhibits improved photocurrent densities than the 1st protonated hematite and the as-prepared sample. It is most likely that the relatively low temperature annealing process did not remove all the introduced protons, instead some of the protons are resistant to the annealing treatment. The 3rd protonated hematite exhibits better performance than the 2nd protonated one, however, the following 3rd annealing treatment does not obviously improve the performance of hematite.

A layer of Co-Pi cocatalyst was photo-electrodeposited on the processed hematite, and the photocurrent density is also shown in Figure 1a. Co-Pi decorated-hematite has a photocurrent density of ~2.7 mA cm⁻² at 1.23 V_{RHE}, and ~3.6 mA cm⁻² at 1.6 V_{RHE}, which is comparable to the benchmark performances previously reported for hematite with different morphologies such as Ti-doped hematite nanoparticles,¹⁹ IrO₂-loaded hematite cauliflowers.⁷ The stability test show that the Co-Pi decorated-hematite has a photocurrent density of ~2.4 mA cm⁻² at 1.23 V_{RHE} after 5 h test (see Figure 1b).

Scanning electron microscopy (SEM) characterization was used to investigate the morphology changes of the as-prepared and treated hematite samples, which were obtained by cutting a single hematite followed by different treatments. Figure 1c-e show the typical features of hematite nanorods, which are similar to previous reports in literature.^{18, 40, 42} Two typical features of nanorods are observed. One type is round and vertical to the substrate, while the other is more elongated and tilted to the substrate. The amount ratios between the two nanorods for these three

samples seem to be not uniform according to the SEM and AFM images (Figure S5), however, a meaningful correlation between this phenomenon and the protonation/annealing treatment cannot be directly made. It is more likely that this discrepancy forms due to the collapse, shrink, and coalescence of β -FeOOH precursors during the high temperature sintering process, which is also one of the reasons that the photocurrents of the as-prepared hematite are not always the same but rather fluctuates in a range. In our experiments, the photocurrent densities of as-prepared hematite at 1.23 V_{RHE} are found in the range of 0.9-1.2 mA cm⁻². In literature, photocurrent densities^{4-5, 17-18} with an even larger dispersion have also been reported between 0.6–1.3 mA cm⁻² for hematite nanorod photoanodes at 1.23 V_{RHE}.

To clarify the effects of protonation and annealing treatment, a control sample was annealed at 120 °C for 1 h without beforehand protonation (Figure S2b). The annealing process alone leads to a slight improvement in the photocurrent densities only at very high potentials, and the onset potential remains the same. In the second round treatment, both protonation and annealing were applied, and then a smaller onset potential and higher photocurrent are observed.

The change tendencies of photocurrents after protonation and annealing treatment are consistent for different samples, in spite of the fluctuated initial photocurrents, as shown in Figure 1, S1 and S2. Therefore, it would still be plausible to conclude that this protonation-annealing treatment is an effective strategy to enhance the performances for hematite photoanode.

3.2. Photocurrents of water and H₂O₂ oxidation. To understand the effects of protonation and annealing treatment on hematite, H₂O₂ was used as hole scavenger in electrolyte. The oxidation of H₂O₂ is thermodynamically more facile than oxidation of water, and has a rate constant 10-100 times higher than that of water.²³ Thus the oxidation of H₂O₂ is considered as a

process with minimal losses of holes at the surface, reflecting mainly the bulk charge separation properties of hematite. A smaller gap between the oxidation photocurrents of H₂O₂ and H₂O indicates less surface recombination of charge carriers.

It is noteworthy that the same hematite (before loading Co-Pi) as in Figure 1 was used to probe the photocurrent densities for H₂O₂ oxidation. Figure 2a-c show the comparisons between the photocurrent densities of H₂O₂ and water oxidation for as-prepared, protonated and annealed hematite. The gap between the photocurrent densities of H₂O₂ oxidation and H₂O oxidation increases in the following order: annealed < as-prepared < protonated, indicating that the protonated sample suffers from the most severe losses of holes at the surface or close to the surface, while the annealed hematite has the lowest surface recombination.

The bulk charge efficiency can be obtained by dividing the photocurrent $J_{\text{H}_2\text{O}_2}$ over J_{abs} (absorption derived maximum photocurrent) assuming the charge injection efficiency is 100% in the presence of H₂O₂.²³ J_{abs} was calculated by integrating the light absorption of each sample with respect to AM 1.5G spectrum. The bulk charge separation efficiency is thus calculated and plotted in Figure 2d. Clearly, the protonated and annealed hematite both have enhanced charge separation efficiency in the bulk, while the former has the highest value, most likely due to higher majority carrier transport and lower bulk recombination. This reduced bulk recombination has been observed on rutile TiO₂ nanoparticle electrodes,³¹ and explained by the reduction of deep electron traps at the grain boundary as a result of proton incorporation.

To summarize, the protonation improves the bulk charge separation efficiency but introduces more surface recombination. The annealing treatment can reduce the surface recombination at the

sacrifice of certain bulk properties, although it still has higher charge separation efficiency than the as-prepared hematite.

3.3. Impedance spectroscopy measurements under light. Impedance spectroscopy were measured under AM 1.5G illumination (100 mW cm^{-2}) to further understand the effects of protonation and annealing on the bulk electron transport and solid-electrolyte interface charge transfer processes. Figure 3a shows the Nyquist plots acquired at $1.18 \text{ V}_{\text{RHE}}$ under illumination for as-prepared and processed hematite. The equivalent circuit^{8,13} shown in the inset of Figure 3a was used to fit the data, which includes both the bulk electron transport and solid-electrolyte charge transfer processes. Here the bulk includes both space charge and Helmholtz layers. Figure 3b reports the fitted resistances and time constants for bulk electron transport and interface charge transfer at $1.18 \text{ V}_{\text{RHE}}$.

The protonated hematite has the smallest bulk resistance and time constant, but the largest charge transfer resistance and time constant. This is consistent with the conclusion derived from the analysis of the photocurrent measurements for water and H_2O_2 oxidation that the protonation improves the bulk charge separation efficiency but also introduces more surface recombination. Water oxidation on metal oxide electrodes is believed to proceed from surface hydroxyl intermediate states formed by hole transfer to a surface-coordinated water and a concomitant deprotonation.^{20, 43-45} The extra protons near the surface of the protonated hematite probably inhibit the hole transfer to water, which results in large resistance R_{ct} and time constant $(RC)_{\text{ct}}$ for charge transfer process.

The annealed hematite has the smallest charge transfer resistance and time constant, as well as the second smallest bulk resistance and time constant, which is also in good agreement with the

photocurrent measurements. It is most likely that the annealing process removes mainly the protons near the surface, largely suppressing the surface recombination while still preserving relatively high bulk charge separation efficiency.

Impedance spectra were also collected at 0.98 V_{RHE} (Figure S3a) and the fitted parameters are shown in Figure S3b. The protonated hematite has the largest time constants for both the bulk transport and charge transfer processes, which is consistent with its very low photocurrents at low potentials.

3.4. Mott-Schottky plots. As previously mentioned, some protons may be resistant to the annealing process. If this is true, the donor density of the annealed hematite should be higher than that of as-prepared one. Impedance spectroscopy data measured in dark were fitted according to the equivalent circuit in the inset of Figure 4a, which has been proved to best represent the dark phenomena.⁸ The fitted space charge layer capacitances were used to plot Mott-Schottky curves (Figure 4a), which enables us to obtain the donor density and flat band potential. The details for fitting impedance spectra, calculating donor density and flat band are shown in the Supporting Information.

The donor densities obtained from Mott-Schottky plots are shown in Figure 4b. The as-prepared hematite has a donor density of $1.54 \times 10^{19} \text{ cm}^{-3}$, which is comparable to literature reports on Sn-doped hematite¹⁷ and Si-doped hematite.⁸ Repeated protonation progressively increases the donor density, which rises up to $4.48 \times 10^{19} \text{ cm}^{-3}$ after the 3rd protonation, contributing to the high conductivity and charge separation efficiency in bulk for protonated hematite. The 3rd annealed hematite still has higher donor densities than the as-prepared hematite. This confirms that residual

protons are present in the annealed hematite, probably due to higher removal energy barriers of the protons in the bulk than those near the surface.

It is noteworthy that the flat band potential slightly shifts to more positive values (downward shift) upon repeated protonation and annealing (Figure 4b). According to eq 1,⁴⁶⁻⁴⁷ the width of the space charge layer W_{sc} under a certain potential V can be obtained when the flat band potential V_{fb} and donor density N_D are known:

$$W_{sc} = \left(\frac{2(V - V_{fb})\epsilon\epsilon_0}{eN_D} \right)^{1/2} \quad (1)$$

The calculated W_{sc} for different samples at 1.23 V_{RHE} are listed in Figure 4b. W_{sc} decreases upon protonation, and increases upon annealing. A thin space charge layer cannot effectively block the back recombination of surface accumulated holes with bulk electrons.⁴⁸ This explains the relatively low photocurrents for water oxidation of the protonated sample at moderately anodic potentials. While at highly positive potentials, the space charge layer becomes wide enough to block the back recombination, leading to similar or higher photocurrents than those measured for the as-prepared hematite.

The influence of oxygen vacancies on the donor density can be ruled out since oxygen vacancy in hematite has very high formation energy of ~20-23 eV,⁴⁹⁻⁵⁰ which makes the formation of extra oxygen vacancy almost impossible at 120 °C. Besides, the minor change in photovoltage (Figure S4) cannot be the main reason for enhanced PEC performance.

3.5. Mechanism discussion. The protonation treatment was conducted under 0.2 V_{RHE} (-0.78 V vs. Ag/AgCl) in 0.5 M NaOH in our experiment. According to the Pourbaix diagram of Fe-H₂O

system,⁵¹ this potential still corresponds to the region of Fe₂O₃(s). Previous reports on the electrochemical reduction of hematite^{34, 39-40} often ascribe the enhancement of photocurrents to the formation of more conductive Fe₃O₄ or even metal Fe. However, more negative potentials (between -1 V and -1.5 V vs. Ag/AgCl or SCE.) were used in these works to reduce hematite, which correspond to the region of Fe₃O₄ or even more reduced phases in Pourbaix diagram. In addition, Cibrev *et al.*⁴⁰ have elaborated the electronic structure changes of hematite after electrochemical reduction through photoemission (PES) and X-ray absorption (XAS) and demonstrated that only potentials more negative than -1.2 V vs. Ag/AgCl are enough to introduce new electronic states in the vicinity of valance band of hematite.

In this work, however, no evidence supports the presence of Fe₃O₄ or more reduced phases of iron. Figure 5 shows XPS, Raman and Mössbauer spectra for as-prepared and treated hematite. No obvious differences are observed between the as-prepared, protonated and annealed hematite for all the spectra. XPS spectra show that binding energies of Fe 2p_{3/2} and Fe 2p_{1/2} are 710.3 eV and 723.6 eV, respectively, along with a typical satellite peak at 718.5 eV, which is characteristic of Fe³⁺.^{40, 52} However, no shoulder close to the Fe 2p_{3/2} peak corresponding to the presence of Fe²⁺ was detected after the protonation or annealing treatments. Raman and Mössbauer spectra are also virtually the same for as-prepared, protonated and annealed hematite, only showing the characteristics of Fe₂O₃. Besides, XRD patterns in Figure S6 also confirm that crystallographic structures are identical for as-prepared and treated hematite. All these evidences verify that our electrochemical reduction do not involve the formation of magnetite Fe₃O₄ or metal Fe.

Based on the above discussions, it would be justified to draw the conclusion that the enhancement of photocurrents in this work is related with protons instead of the reduction of Fe₂O₃.

A new mechanism is proposed for this work to explain the protonation process of hematite, which can be written similar to the Volmer equation:⁵³⁻⁵⁴



Protons can be adsorbed onto or intercalated into hematite, which simultaneously introduces electrons into Fe_2O_3 and generates OH^- ions in the local region. Here electrons increase the donor density in the bulk of hematite, which is reflected by the improved charge separation efficiency and conductivity in bulk for protonated hematite. But protons near the surface may also act as recombination centers thus deteriorate the photocurrent under relatively low bias. It is found that a low temperature annealing treatment can recover the surface properties. This has never been reported in literature. We thus proposed a combined protonation-annealing treatment for hematite. After annealing treatment, extra protons on the surface were removed and thus the surface recombination was also impressed.

Furthermore, previous reports on electrochemical reduction of hematite used sample prepared under a relatively low temperature of $550\text{ }^\circ\text{C}$ ³⁴ or $600\text{ }^\circ\text{C}$ ³⁹⁻⁴⁰, which have very low photoactivity. For hematite with low donor densities, the electrochemical reduction of hematite can improve the photocurrents for water splitting through the enhancement of the majority carrier transport. Still, photocurrent densities of less than 1 mA cm^{-2} are reported for optimized pretreated hematite at $1.23\text{ V}_{\text{RHE}}$ in these works.^{34, 39-40} In our work, however, an additional activation treatment by sintering hematite at $800\text{ }^\circ\text{C}$ for 10 min was adopted to enable the diffusion of Sn from fluorine-doped SnO_2 (FTO) substrate to hematite.^{4-5, 16-18} Therefore, this work used highly-doped hematite, which is also verified by the much higher photocurrents in our case. Although Shangguan *et al.*³⁴ also reported a Ti-doped hematite, the annealing treatment under $550\text{ }^\circ\text{C}$ seems inefficient to

incorporate enough Ti^{4+} in the crystalline structure of hematite, which shows a very low photocurrent of $\sim 400 \mu\text{A cm}^{-2}$ at $1.23 \text{ V}_{\text{RHE}}$ in comparison to 1.8 mA cm^{-2} in our case. Therefore, it is worth noting that our new understanding on the protonation treatment is based on hematite with sufficiently high donor density.

4. CONCLUSIONS

In conclusion, repeated protonation and annealing treatments can cathodically shift the onset potential and improve photocurrents for hematite photoanode. Literature often ascribe the enhancement in performance to the formation of Fe_3O_4 or metal Fe, however, it is demonstrated that the enhancement is mainly related with the incorporation of proton/ e^- in this work. Protons and electrons are incorporated into hematite in a way similar to Volmer reaction. The protonation process increases the donor density, reduces bulk electron traps but introduces more surface recombination. The subsequent low temperature annealing removes extra protons near the surface to suppress surface recombination while preserving relatively high bulk charge separation efficiency. For oxides with low donor densities, a negative polarization alone can improve the photocurrents for water splitting through the enhancement of the majority carrier transport, as in the case of low-doped Fe_2O_3 .^{34, 39-40} However, for oxides with a sufficiently high donor density, further increasing the donor density will reduce the photocurrents due to the increased recombination near the surface. Our measurements show that a low temperature annealing treatment can improve the surface properties while keeping a low bulk recombination.

■ ASSOCIATED CONTENT

●, Supporting Information

The Supporting Information is available free of charge on the ACS Publications website at DOI: 10.1021/acsami.xxxxxx.

Additional experimental details including optimization of annealing parameters, photograph of hematite, photocurrents for anneal-only hematite, Nyquist plot under light at 0.98 V_{RHE}, open circuit potentials, electrochemical surface area, photovoltage calculations, Pourbaix diagram, AFM images and XRD patterns. (PDF)

■ AUTHOR INFORMATION

Corresponding Author

* siwp86@gmail.com; thomas.lippert@psi.ch

Notes

The authors declare no competing financial interest.

■ ACKNOWLEDGEMENTS

This research is supported by the Paul Scherrer Institute and the NCCR MARVEL, funded by the Swiss National Science Foundation. We thank U. Aschauer for discussions of the results, A.

Palla-Papavlu, M. El Kazzi, J. Landers and H. Wende for kind help with experiments.

■ REFERENCES

- (1). Fujishima, A.; Honda, K., Electrochemical photolysis of water at a semiconductor electrode. *Nature* **1972**, *238*, 37-38.
- (2). Gratzel, M., Photoelectrochemical cells. *Nature* **2001**, *414*, 338-344.
- (3). Sivula, K.; Zboril, R.; Le Formal, F.; Robert, R.; Weidenkaff, A.; Tucek, J.; Frydrych, J.; Grätzel, M., Photoelectrochemical water splitting with mesoporous hematite prepared by a solution-based colloidal approach. *J. Am. Chem. Soc.* **2010**, *132*, 7436-7444.
- (4). Jang, J.-W.; Du, C.; Ye, Y.; Lin, Y.; Yao, X.; Thorne, J.; Liu, E.; McMahon, G.; Zhu, J.; Javey, A.; Guo, J.; Wang, D., Enabling unassisted solar water splitting by iron oxide and silicon. *Nat. Commun.* **2015**, *6*, 7447.

- (5). Kim, J. Y.; Youn, D. H.; Kang, K.; Lee, J. S., Highly conformal deposition of an ultrathin FeOOH layer on a hematite nanostructure for efficient solar water splitting. *Angew. Chem. Int. Ed.* **2016**, *55*, 10854-10858.
- (6). Wheeler, D. A.; Wang, G.; Ling, Y.; Li, Y.; Zhang, J. Z., Nanostructured hematite: synthesis, characterization, charge carrier dynamics, and photoelectrochemical properties. *Energy Environ. Sci.* **2012**, *5*, 6682-6702.
- (7). Tilley, S. D.; Cornuz, M.; Sivula, K.; Grätzel, M., Light-induced water splitting with hematite: improved nanostructure and iridium oxide catalysis. *Angew. Chem. Int. Ed.* **2010**, *49*, 6405-6408.
- (8). Cesar, I.; Sivula, K.; Kay, A.; Zboril, R.; Grätzel, M., Influence of feature size, film thickness, and silicon doping on the performance of nanostructured hematite photoanodes for solar water splitting. *J. Phys. Chem. C* **2009**, *113*, 772-782.
- (9). Moniz, S. J. A.; Shevlin, S. A.; Martin, D. J.; Guo, Z.-X.; Tang, J., Visible-light driven heterojunction photocatalysts for water splitting - a critical review. *Energy Environ. Sci.* **2015**, *8*, 731-759.
- (10). Kim, J. Y.; Jang, J.-W.; Youn, D. H.; Magesh, G.; Lee, J. S., A Stable and Efficient Hematite Photoanode in a Neutral Electrolyte for Solar Water Splitting: Towards Stability Engineering. *Adv. Energy Mater.* **2014**, *4*, 1400476.
- (11). Yu, Q.; Meng, X.; Wang, T.; Li, P.; Ye, J., Hematite Films Decorated with Nanostructured Ferric Oxyhydroxide as Photoanodes for Efficient and Stable Photoelectrochemical Water Splitting. *Adv. Funct. Mater.* **2015**, *25*, 2686-2692.
- (12). Steier, L.; Herraiz-Cardona, I.; Gimenez, S.; Fabregat-Santiago, F.; Bisquert, J.; Tilley, S. D.; Grätzel, M., Understanding the Role of Underlayers and Overlayers in Thin Film Hematite Photoanodes. *Adv. Funct. Mater.* **2014**, *24*, 7681-7688.
- (13). Sivula, K.; Le Formal, F.; Grätzel, M., Solar water splitting: progress using hematite (α -Fe₂O₃) photoelectrodes. *ChemSusChem* **2011**, *4*, 432-449.
- (14). Warren, S. C.; Voitchovsky, K.; Dotan, H.; Leroy, C. M.; Cornuz, M.; Stellacci, F.; Hébert, C.; Rothschild, A.; Grätzel, M., Identifying champion nanostructures for solar water-splitting. *Nat. Mater.* **2013**, *12*, 842-849.
- (15). Marusak, L. A.; Messier, R.; White, W. B., Optical absorption spectrum of hematite, α -Fe₂O₃ near IR to UV. *J. Phys. Chem. Solids* **1980**, *41*, 981-984.
- (16). Li, C.; Li, A.; Luo, Z.; Zhang, J.; Chang, X.; Huang, Z.; Wang, T.; Gong, J., Surviving high-temperature calcination: ZrO₂-induced hematite nanotubes for photoelectrochemical water oxidation. *Angew. Chem. Int. Ed.* **2017**, *56*, 4150-4155.
- (17). Ling, Y.; Wang, G.; Wheeler, D. A.; Zhang, J. Z.; Li, Y., Sn-doped hematite nanostructures for photoelectrochemical water splitting. *Nano Lett.* **2011**, *11*, 2119-2125.
- (18). Kim, J. Y.; Magesh, G.; Youn, D. H.; Jang, J.-W.; Kubota, J.; Domen, K.; Lee, J. S., Single-crystalline, wormlike hematite photoanodes for efficient solar water splitting. *Sci. Rep.* **2013**, *3*, 2681.
- (19). Wang, G.; Ling, Y.; Wheeler, D. A.; George, K. E. N.; Horsley, K.; Heske, C.; Zhang, J. Z.; Li, Y., Facile synthesis of highly photoactive α -Fe₂O₃-based films for water oxidation. *Nano Lett.* **2011**, *11*, 3503-3509.
- (20). Upul Wijayantha, K. G.; Saremi-Yarahmadi, S.; Peter, L. M., Kinetics of oxygen evolution at α -Fe₂O₃ photoanodes: a study by photoelectrochemical impedance spectroscopy. *Phys. Chem. Chem. Phys.* **2011**, *13*, 5264-5270.

- (21). Zandi, O.; Hamann, T. W., Determination of photoelectrochemical water oxidation intermediates on hematite electrode surfaces using operando infrared spectroscopy. *Nat. Chem.* **2016**, *8*, 778-783.
- (22). Le Formal, F.; Tetreault, N.; Cornuz, M.; Moehl, T.; Gratzel, M.; Sivula, K., Passivating surface states on water splitting hematite photoanodes with alumina overlayers. *Chem. Sci.* **2011**, *2*, 737-743.
- (23). Dotan, H.; Sivula, K.; Gratzel, M.; Rothschild, A.; Warren, S. C., Probing the photoelectrochemical properties of hematite α -Fe₂O₃ electrodes using hydrogen peroxide as a hole scavenger. *Energy Environ. Sci.* **2011**, *4*, 958-964.
- (24). Ding, C.; Wang, Z.; Shi, J.; Yao, T.; Li, A.; Yan, P.; Huang, B.; Li, C., Substrate-Electrode Interface Engineering by an Electron-Transport Layer in Hematite Photoanode. *ACS Appl. Mat. Interfaces* **2016**, *8*, 7086-7091.
- (25). Marelli, M.; Naldoni, A.; Minguzzi, A.; Allieta, M.; Virgili, T.; Scavia, G.; Recchia, S.; Psaro, R.; Dal Santo, V., Hierarchical Hematite Nanoplatelets for Photoelectrochemical Water Splitting. *ACS Appl. Mat. Interfaces* **2014**, *6*, 11997-12004.
- (26). Zhang, Y.; Jiang, S.; Song, W.; Zhou, P.; Ji, H.; Ma, W.; Hao, W.; Chen, C.; Zhao, J., Nonmetal P-doped hematite photoanode with enhanced electron mobility and high water oxidation activity. *Energy Environ. Sci.* **2015**, *8*, 1231-1236.
- (27). Ahn, H. J.; Yoon, K. Y.; Kwak, M. J.; Jang, J. H., A Titanium - Doped SiO_x Passivation Layer for Greatly Enhanced Performance of a Hematite - Based Photoelectrochemical System. *Angew. Chem. Int. Ed.* **2016**, *55*, 9922-9926.
- (28). Yang, X.; Liu, R.; Du, C.; Dai, P.; Zheng, Z.; Wang, D., Improving Hematite-based Photoelectrochemical Water Splitting with Ultrathin TiO₂ by Atomic Layer Deposition. *ACS Appl. Mat. Interfaces* **2014**, *6*, 12005-12011.
- (29). Li, C.; Wang, T.; Luo, Z.; Liu, S.; Gong, J., Enhanced Charge Separation through ALD-Modified Fe₂O₃/Fe₂TiO₅ Nanorod Heterojunction for Photoelectrochemical Water Oxidation. *Small* **2016**, *12*, 3415-3422.
- (30). Zhao, J.; Olide, E.; Osterloh, F. E., Enhancing majority carrier transport in WO₃ water oxidation photoanode via electrochemical doping. *J. Electrochem. Soc.* **2015**, *162*, H65-H71.
- (31). Jiménez, J. M.; Bourret, G. R.; Berger, T.; McKenna, K. P., Modification of charge trapping at particle/particle interfaces by electrochemical hydrogen doping of nanocrystalline TiO₂. *J. Am. Chem. Soc.* **2016**, *138*, 15956-15964.
- (32). Wang, Q.; Zhang, Z.; Zakeeruddin, S. M.; Grätzel, M., Enhancement of the performance of dye-sensitized solar cell by formation of shallow transport levels under visible light illumination. *J. Phys. Chem. C* **2008**, *112*, 7084-7092.
- (33). Fabregat-Santiago, F.; Barea, E. M.; Bisquert, J.; Mor, G. K.; Shankar, K.; Grimes, C. A., High carrier density and capacitance in TiO₂ nanotube arrays induced by electrochemical doping. *J. Am. Chem. Soc.* **2008**, *130*, 11312-11316.
- (34). Shangguan, P.; Tong, S.; Li, H.; Leng, W., Enhanced photoelectrochemical oxidation of water over undoped and Ti-doped α -Fe₂O₃ electrodes by electrochemical reduction pretreatment. *RSC Adv.* **2013**, *3*, 10163-10167.
- (35). Li, H.; Chen, Z.; Tsang, C. K.; Li, Z.; Ran, X.; Lee, C.; Nie, B.; Zheng, L.; Hung, T.; Lu, J.; Pan, B.; Li, Y. Y., Electrochemical doping of anatase TiO₂ in organic electrolytes for high-performance supercapacitors and photocatalysts. *J. Mater. Chem. A* **2014**, *2*, 229-236.

- (36). Forney, M. W.; Ganter, M. J.; Staub, J. W.; Ridgley, R. D.; Landi, B. J., Prelithiation of silicon-carbon nanotube anodes for lithium ion batteries by stabilized lithium metal powder (SLMP). *Nano Lett.* **2013**, *13*, 4158-4163.
- (37). Shi, G. A.; Stavola, M.; Pearton, S. J.; Thieme, M.; Lavrov, E. V.; Weber, J., Hydrogen local modes and shallow donors in ZnO. *Phys. Rev. B* **2005**, *72*, 195211.
- (38). King, P. D. C.; Lichti, R. L.; Celebi, Y. G.; Gil, J. M.; Vilão, R. C.; Alberto, H. V.; Pirote Duarte, J.; Payne, D. J.; Egdell, R. G.; McKenzie, I.; McConville, C. F.; Cox, S. F. J.; Veal, T. D., Shallow donor state of hydrogen in In₂O₃ and SnO₂: implications for conductivity in transparent conducting oxides. *Phys. Rev. B* **2009**, *80*, 081201.
- (39). Wang, J.; Waters, J. L.; Kung, P.; Kim, S. M.; Kelly, J. T.; McNamara, L. E.; Hammer, N. I.; Pemberton, B. C.; Schmehl, R. H.; Gupta, A.; Pan, S., A Facile Electrochemical Reduction Method for Improving Photocatalytic Performance of α -Fe₂O₃ Photoanode for Solar Water Splitting. *ACS Appl. Mat. Interfaces* **2017**, *9*, 381-390.
- (40). Cibrev, D.; Tallarida, M.; Das, C.; Lana-Villarreal, T.; Schmeisser, D.; Gómez, R., New insights into water photooxidation on reductively pretreated hematite photoanodes. *Phys. Chem. Chem. Phys.* **2017**, *19*, 21807-21817.
- (41). Vayssieres, L.; Beermann, N.; Lindquist, S.-E.; Hagfeldt, A., Controlled aqueous chemical growth of oriented three-dimensional crystalline nanorod arrays: application to iron(III) oxides. *Chem. Mater.* **2001**, *13*, 233-235.
- (42). Ling, Y.; Wang, G.; Reddy, J.; Wang, C.; Zhang, J. Z.; Li, Y., The Influence of Oxygen Content on the Thermal Activation of Hematite Nanowires. *Angew. Chem. Int. Ed.* **2012**, *51*, 4074-4079.
- (43). Salvador, P., Influence of pH on the potential dependence of the efficiency of water photo-oxidation at n-TiO₂ Electrodes. *J. Electrochem. Soc.* **1981**, *128*, 1895-1900.
- (44). Cook, T. R.; Dogutan, D. K.; Reece, S. Y.; Surendranath, Y.; Teets, T. S.; Nocera, D. G., Solar energy supply and storage for the legacy and nonlegacy worlds. *Chem. Rev.* **2010**, *110*, 6474-6502.
- (45). Klahr, B.; Gimenez, S.; Fabregat-Santiago, F.; Hamann, T.; Bisquert, J., Water oxidation at hematite photoelectrodes: the role of surface states. *J. Am. Chem. Soc.* **2012**, *134*, 4294-4302.
- (46). Iandolo, B.; Wickman, B.; Zoric, I.; Hellman, A., The rise of hematite: origin and strategies to reduce the high onset potential for the oxygen evolution reaction. *J. Mater. Chem. A* **2015**, *3*, 16896-16912.
- (47). Peter, L. M., Photoelectrochemistry: From Basic Principles To Photocatalysis. In *Photocatalysis: Fundamentals and Perspectives*, The Royal Society of Chemistry: **2016**; Chapter 1, pp 1-28.
- (48). Le Formal, F.; Pendlebury, S. R.; Cornuz, M.; Tilley, S. D.; Grätzel, M.; Durrant, J. R., Back electron-hole recombination in hematite photoanodes for water splitting. *J. Am. Chem. Soc.* **2014**, *136*, 2564-2574.
- (49). Warschkow, O.; Ellis, D. E.; Hwang, J.; Mansourian-Hadavi, N.; Mason, T. O., Defects and charge transport near the hematite (0001) surface: an atomistic study of oxygen vacancies. *J. Am. Ceram. Soc.* **2002**, *85*, 213-220.
- (50). Catlow, C. R. A.; Corish, J.; Hennessy, J.; Mackrodt, W. C., Atomistic simulation of defect structures and ion transport in α -Fe₂O₃ and α -Cr₂O₃. *J. Am. Ceram. Soc.* **1988**, *71*, 42-49.
- (51).

https://chem.libretexts.org/Bookshelves/Inorganic_Chemistry/Book%3A_Inorganic_Che

mistry_(Wikibook)/Chapter_04%3A_Redox_Stability_and_Redox_Reactions/4.5%3A_Pourbaix_diagrams).

(52). Yamashita, T.; Hayes, P., Analysis of XPS spectra of Fe²⁺ and Fe³⁺ ions in oxide materials. *Appl. Surf. Sci.* **2008**, *254*, 2441-2449.

(53). Conway, B. E.; Tilak, B. V., Interfacial processes involving electrocatalytic evolution and oxidation of H₂, and the role of chemisorbed H. *Electrochim. Acta* **2002**, *47*, 3571-3594.

(54). Krstajić, N.; Popović, M.; Grgur, B.; Vojnović, M.; Šepa, D., On the kinetics of the hydrogen evolution reaction on nickel in alkaline solution: Part I. The mechanism. *J. Electroanal. Chem.* **2001**, *512*, 16-26.

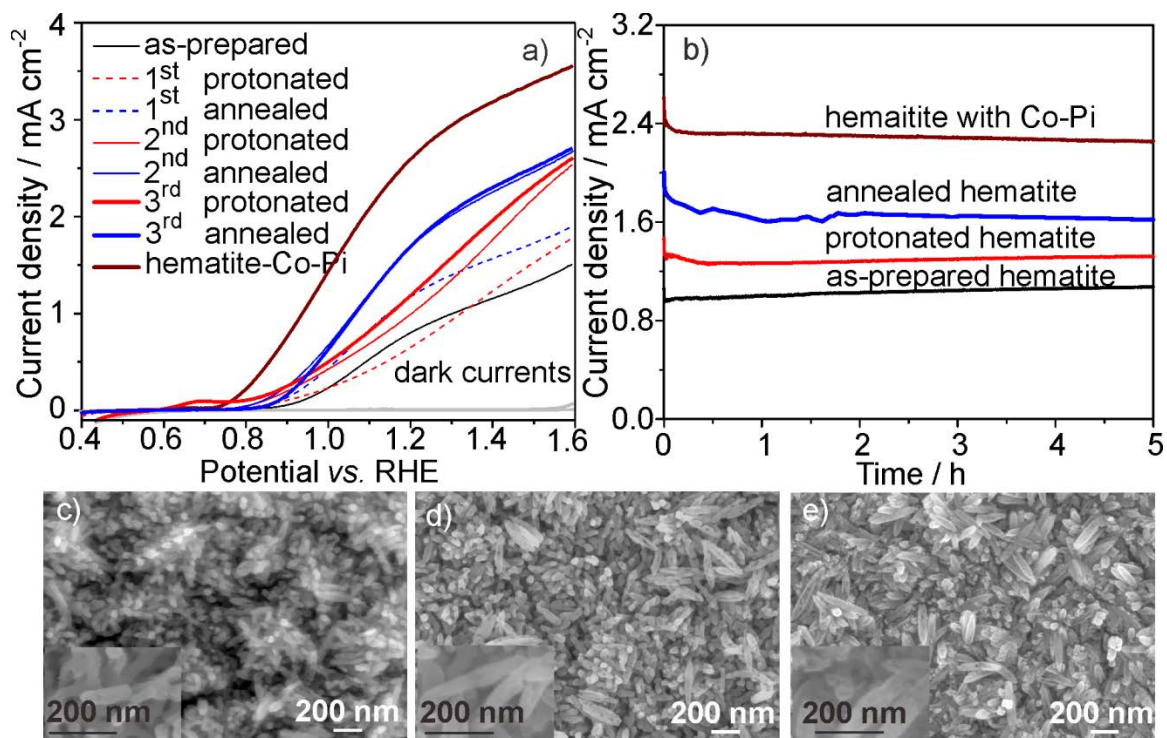


Figure 1. (a) Photocurrent densities of hematite in Ar-saturated 0.5 M NaOH electrolyte (pH=13.0) under AM 1.5G illumination of 100 mW cm^{-2} : as-prepared, the 1st protonated, the 1st annealed at $120 \text{ }^\circ\text{C}$, the 2nd protonated, and the 2nd annealed at $120 \text{ }^\circ\text{C}$, as well as processed hematite with Co-Pi cocatalyst. (b) Photocurrent stability test for protonated, annealed hematite and hematite with Co-Pi cocatalyst. (c-e) SEM images for as-prepared, protonated, and annealed hematite.

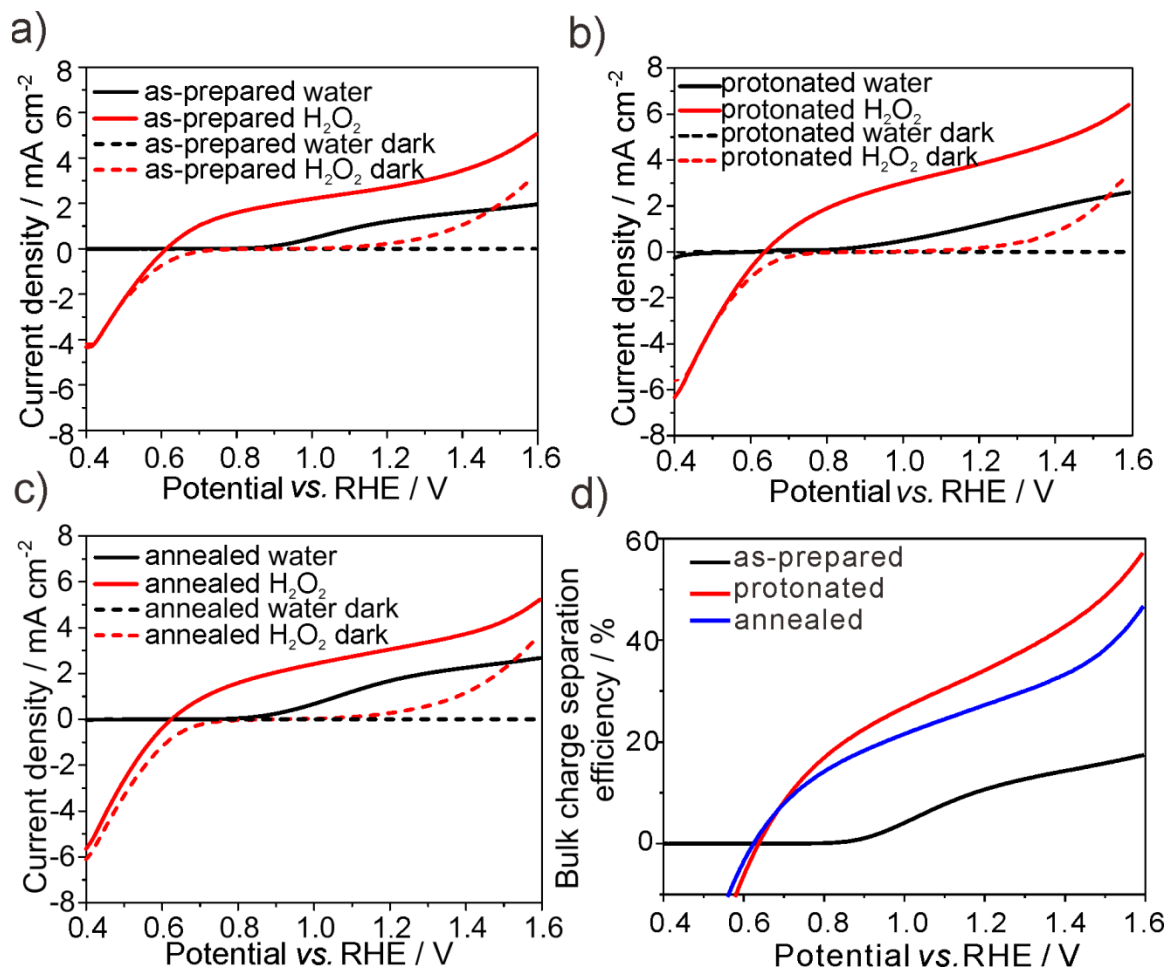


Figure 2. Photocurrent densities of hematite in 0.5M NaOH in the presence of 0.5 M H₂O₂ under AM 1.5G illumination with a power density of 100 mW cm⁻². (a) As-prepared, (b) the 3rd protonated, (c) annealed at 120 °C after the 3rd protonation. (d) The bulk charge separation efficiency for as-prepare, protonated and annealed hematite.

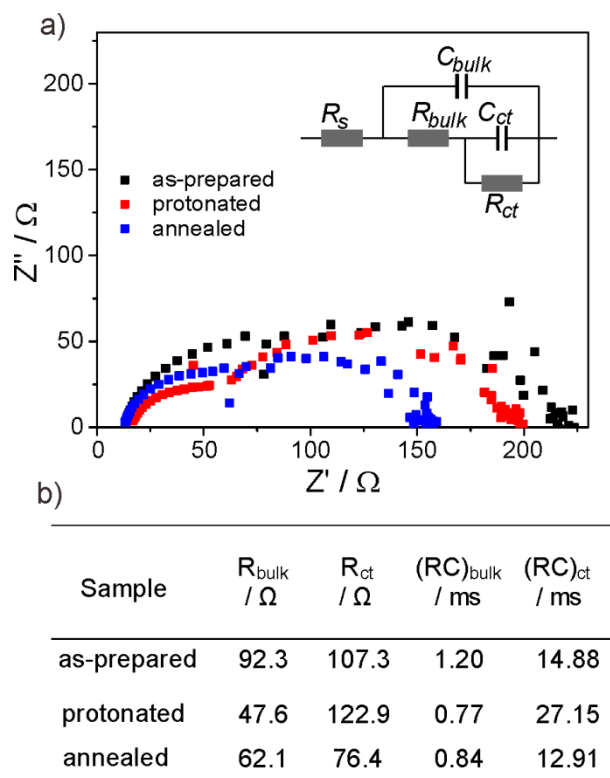


Figure 3. (a) Nyquist plots measured under AM 1.5G illumination at 1.18 V_{RHE} for as-prepared, 3rd protonated and annealed hematite in 0.5 M NaOH electrolyte saturated with O₂ and fitted with the equivalent circuit shown as inset. (b) Bulk transport resistance R_{bulk} and time constant $(RC)_{\text{bulk}}$, hematite-electrolyte charge transfer resistance R_{ct} and time constant $(RC)_{\text{ct}}$, obtained by fitting the impedance spectroscopy data.

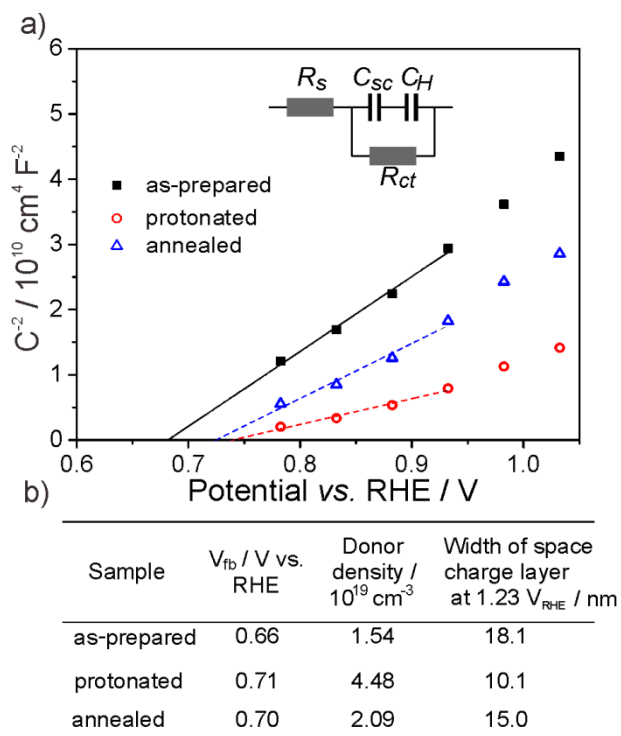


Figure 4. (a) Mott-Schottky plots obtained by measuring the impedance spectroscopy in 0.5 M NaOH electrolyte saturated with O_2 in dark for as-prepared, 3rd protonated and annealed hematite. The complex impedance plane plots were fitted according to the equivalent circuit in the inset. (b) Flat band potential, donor density and the width of space charge layer at $1.23 V_{RHE}$.

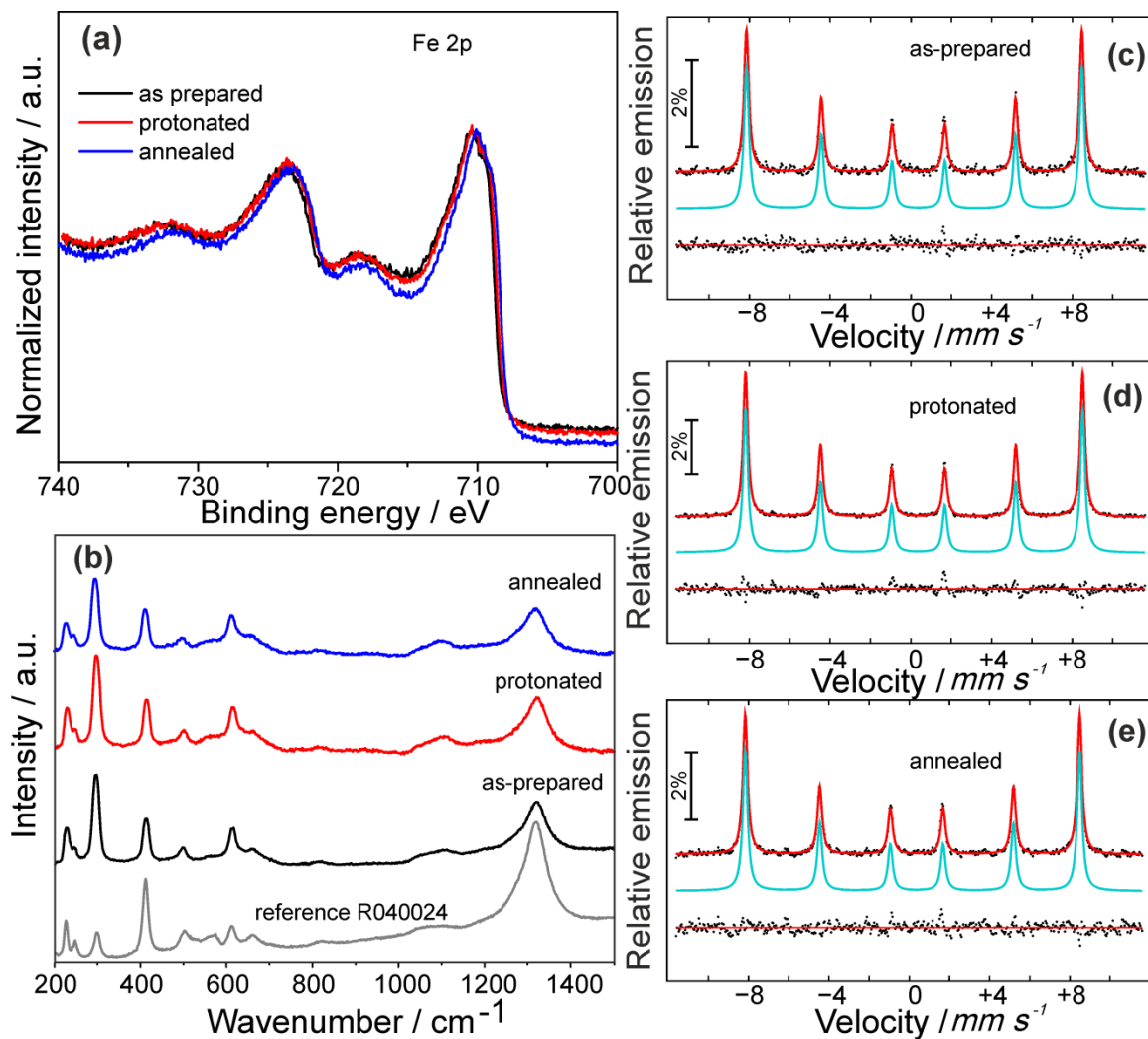


Figure 5. (a) X-ray photoelectron spectroscopy at the surface, (b) Raman and (c) Mössbauer spectroscopy in the bulk for as-prepared, protonated and annealed hematite.